Violation of Matthias rule: Elemental composition as the key determinant of critical temperature in bcc high-entropy superconductors

Rafał Idczak,[1,*] Wojciech Nowak,[1,2] Michał Babij,[2] Daniel Gnida,[2] Robert Konieczny,[1] Monika K. Krawczyk,[1] Dorota Podsiadła,[1] Tomasz Ossowski,[1] Rafał Topolnicki,[1,3] and Adam Pikul[2]

[1]*Institute of Experimental Physics, University of Wrocław, pl. M. Borna 9, 50-204 Wrocław, Poland*

[2]*Institute of Low Temperature and Structure Research, Polish Academy of Sciences, ul. Okólna 2, 50-422 Wrocław, Poland*

[3]*Dioscuri Center in Topological Data Analysis, Institute of Mathematics, Polish Academy of Sciences, ul. Śniadeckich 8, 00-656 Warsaw, Poland*

(Received 22 May 2025; accepted 17 June 2025; published 16 July 2025)

We systematically investigate three body-centred cubic (bcc) high-entropy alloys (HEAs) with an identical valence electron count (VEC = 4.375): $(NbHf)_{0.75}(TiZr)_{0.25}$, $(NbZr)_{0.75}(TiHf)_{0.25}$, and $(NbTi)_{0.75}(ZrHf)_{0.25}$. Despite their isoelectronic nature, it was found that these alloys exhibit markedly different superconducting properties. Critical temperatures T_c range from 7.14(5) K to 8.17(5) K, while upper critical fields $\mu_0 H_{c2}(0)$ exceed 12 T, reaching 14.0(9) T for the Ti-rich alloy $(NbTi)_{0.75}(ZrHf)_{0.25}$. These variations highlight the limited predictive power of the Matthias rule in HEA design. Furthermore, the exceptional properties observed in the Ti-rich composition suggest that Nb and Ti are critical elements for the development of new HEAs for next-generation superconducting magnets.

DOI: 10.1103/fnz7-bzmw

I. INTRODUCTION

High-entropy alloys (HEAs) are multicomponent systems characterized by near-equimolar compositions of several principal elements. Despite their compositional complexity, these alloys frequently crystallize in simple structures, a phenomenon attributed to the high configurational entropy arising from the random distribution of constituent elements across lattice sites [1,2]. The first superconducting HEA, $Ta_{0.34}Nb_{0.33}Hf_{0.08}Zr_{0.14}Ti_{0.11}$, was discovered in 2014 [3], highlighting the potential of HEA in practical applications. Notably, superconducting HEAs combine bulk superconductivity with exceptional mechanical properties, including high specific strength, thermal stability, and cryogenic fracture toughness, rendering them promising candidates for next-generation superconducting magnets [4–6].

The elemental composition of body-centered cubic (bcc) high-entropy alloys is critical in determining their superconducting properties. Empirical trends in crystalline transition-metal superconductors, commonly known as the Matthias rule, predict an optimal superconducting transition temperature (T_c) at a valence electron count (VEC) of 4.67 [7]. Since that, deviations from the optimal VEC range may significantly suppress the superconducting transition temperature. Recent studies suggest that this correlation extends to bcc-type HEA superconductors, where VEC not only governs T_c but also directly impacts phase stability [4,8,9]. For instance, BCC phases are stabilized within a VEC range of 3.2–5.2, while HEAs with higher VEC values crystallize in various structures, including the face centered cubic (fcc), CsCl-type, α-Mn, and hexagonal close-packed (hcp) structures. It is worth noting here, that despite the fact that most bcc-type HEAs with VEC close to 4.67 have $T_c > 7$ K, the systematic investigations on isoelectronic replacements, using Mo-Y, Mo-Sc, and Cr-Sc mixtures, in Ta-Nb-Zr-Hf-Ti HEA reveal that isoelectronic substitution of niobium or tantalum reduces T_c by more than 60%, whereas analogous replacements of hafnium, zirconium, or titanium have a limited impact on the critical temperature [10]. Therefore, these observations suggest that T_c strongly depends on the elemental makeup of the alloy, not exclusively its electron count.

To evaluate this hypothesis, we systematically investigate three bcc-type HEAs: $(NbHf)_{0.75}(TiZr)_{0.25}$, $(NbZr)_{0.75}(TiHf)_{0.25}$, and $(NbTi)_{0.75}(ZrHf)_{0.25}$. The selected compositions maintain an isoelectronic valence electron count (VEC = 4.375) while varying the local chemical environments of the constituent d-electron species. The alloys were comprehensively characterized through magnetization and specific heat measurements, enabling direct comparison of their superconducting properties and allowing assessment of composition-dependent superconducting behavior independent of electron count. In addition, our experimental results were supported by first-principles density functional theory (DFT) calculations, which provide fundamental insights into the electronic structure of the investigated HEAs.

II. EXPERIMENTAL AND COMPUTATIONAL DETAILS

Polycrystalline samples of $(NbHf)_{0.75}(TiZr)_{0.25}$, $(NbZr)_{0.75}(TiHf)_{0.25}$, and $(NbTi)_{0.75}(ZrHf)_{0.25}$ were synthesized via arc

*Contact author: rafal.idczak@uwr.edu.pl

melting in a water-cooled copper crucible under a Ti-gettered argon atmosphere. Stoichiometric quantities of high-purity constituent elements were melted and remelted five times to ensure chemical homogeneity, with each ingot flipped between melting cycles to promote uniform composition. The total weight loss after the synthesis was less than 0.3%.

The crystal structure of the synthesized alloys were characterized by x-ray diffraction (XRD) using a PANalytical X'Pert Pro diffractometer equipped with a CuK_α radiation source. The resulting XRD patterns were analysed using the Rietveld method implemented in the FULLPROF software [11].

Specific heat and magnetic properties were measured using a Quantum Design PPMS platform at temperatures down to 1.9 K and in applied external magnetic fields of up to 9.0 T.

Electronic structure calculations employed two complementary methods. First, the Korringa-Kohn-Rostoker Coherent Potential Approximation (KKR-CPA) formalism [12–16] was implemented via the AKAIKKR package [17–19]. The semi-relativistic muffin-tin potential used the PBE exchange-correlation functional [20–22], with an angular momentum cutoff $l_{\max} = 3$ and 5216 k-points sampling the irreducible Brillouin zone for self-consistency and density of states calculations. KKR-CPA calculations were performed both in atomic sphere approximation (ASA) and using more general muffin-tin (MT) potentials, as the MT approach better accounts for nonspherical potential variations making it more suitable for alloy systems. For each system, the equilibrium lattice parameter a, bulk modulus B, and its pressure derivative B' were derived from Birch-Murnaghan equation of state fits [23]. Complementary DFT calculations were performed using the VIENNA AB INITIO SIMULATION PACKAGE (VASP) [24–26], employing: projector augmented-wave (PAW) potentials [27,28] for electron-ion interactions; the Perdew-Burke-Ernzerhof (PBE) generalized gradient approximation (GGA) for exchange-correlation effects; a 400-V plane-wave cutoff energy and 3×3×3 supercells (54 atoms) with three random atomic configurations to model chemical disorder. The supercells are composed of Ti, Nb, Hf, and Zr atoms randomly distributed on bcc lattice sites in the exact stoichiometry of the studied HEAs. For all three configurations a, B, and B' were derived using the Birch-Murnaghan equation of state.

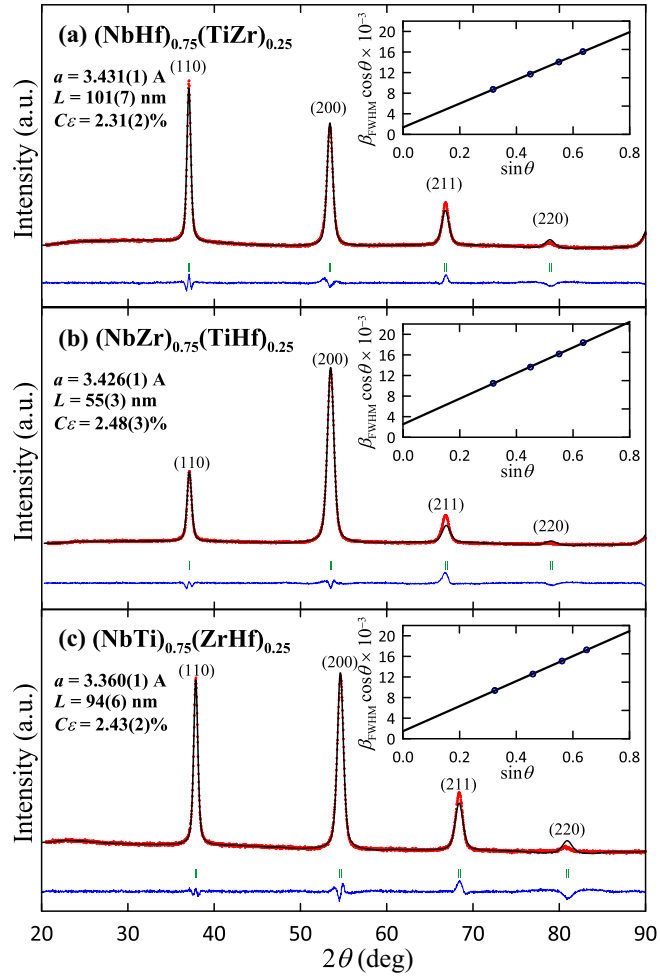

FIG. 1. X-ray powder diffraction patterns of (a) $(NbHf)_{0.75}(TiZr)_{0.25}$, (b) $(NbZr)_{0.75}(TiHf)_{0.25}$, and (c) $(NbTi)_{0.75}(ZrHf)_{0.25}$ measured at room temperature. The experimental data are denoted by red points, while the corresponding Rietveld refinement is shown as a black line. The Bragg peak positions for the identified bcc phase are marked by vertical green tick marks below the pattern. The residual difference between observed and calculated intensities is plotted as a blue line. Inset shows the Williamson-Hall plot with a linear fit to data points.

III. RESULTS AND DISCUSSION

A. Crystal structure and chemical composition

Figure 1 presents XRD patterns measured at room temperature for $(NbHf)_{0.75}(TiZf)_{0.25}$, $(NbZr)_{0.75}(TiHf)_{0.25}$, and $(NbTi)_{0.75}(ZrHf)_{0.25}$ samples. As one can notice, all prepared alloys are found to be single phase with broad reflections, which can be attributed to the high degree of disorder present in the HEAs as well as the nonideal diffraction sample preparation (diffraction experiments were conducted using bulk specimens, not powders). Analysis of the experimental data using the Rietveld method revealed that this phase can be described as a bcc structure (space group $Im\bar{3}m$, W-type structure). The lattice parameters a for $(NbTi)_{0.75}(ZrHf)_{0.25}$, $(NbZr)_{0.75}(TiHf)_{0.25}$, and $(NbHf)_{0.75}(TiZr)_{0.25}$ are determined to be 3.360(1) Å, 3.426(1) Å, and 3.431(1) Å, respectively. The lattice parameters show a systematic increase with alloy molar mass and are comparable with the previously reported values for variants of Ta-Nb-Hf-Zr-Ti high-entropy alloy [3,8,29].

The insets in Fig. 1 display the Williamson-Hall plots calculated for each alloy according to the equation [30]

$$\beta_{\mathrm{FWHM}} \cos\theta = C\epsilon \sin\theta + \frac{K\lambda}{L}, \tag{1}$$

where β_{FWHM} is the line broadening at half maximum intensity, λ is the wavelength of the x-rays used in the experiment, K stands for the dimensionless shape factor and θ denotes the Bragg angle. Assuming a typical value of $K = 0.9$ for cubic symmetry systems, the mean grain size L and the level of internal strain $C\epsilon$ were determined to be 101(7) nm and 2.31(2)%, respectively, for the polycrystalline $(NbHf)_{0.75}(TiZr)_{0.25}$ alloy. Comparable values were obtained

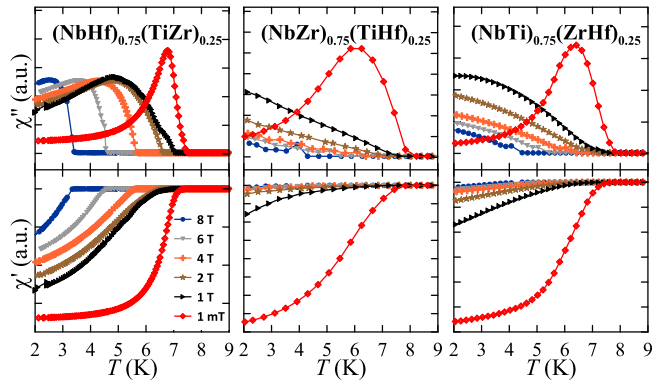

FIG. 2. The temperature dependencies of real χ' and imaginary χ'' parts of ac magnetic susceptibility measured for $(NbHf)_{0.75}(TiZr)_{0.25}$, $(NbZr)_{0.75}(TiHf)_{0.25}$, and $(NbTi)_{0.75}(ZrHf)_{0.25}$ in various magnetic fields up to $\mu_0 H = 8$ T.

for $(NbTi)_{0.75}(ZrHf)_{0.25}$, with $L = 94(6)$ nm and $C\epsilon = 2.43(2)\%$. In contrast, $(NbZr)_{0.75}(TiHf)_{0.25}$ exhibits a significantly smaller grain size [$L = 55(3)$ nm] and a slightly higher internal strain [$C\epsilon = 2.48(3)\%$], indicating the presence of finer grains and greater lattice distortion in this alloy.

B. Superconductivity

Figure 2 presents the ac magnetic susceptibility of $(NbHf)_{0.75}(TiZr)_{0.25}$, $(NbZr)_{0.75}(TiHf)_{0.25}$, and $(NbTi)_{0.75}(ZrHf)_{0.25}$ measured between 2 to 9 K under applied magnetic fields up to $\mu_0 H = 8$ T. In the case of $(NbHf)_{0.75}(TiZr)_{0.25}$, the real component ($\chi'$) measured at $\mu_0 H = 1$ mT unveils the onset of a diamagnetic signal below 7.3(1) K, while the simultaneous emergence of a nonzero imaginary component (χ'') below this temperature confirms the onset of bulk superconductivity at $T_c^{mag} = 7.3(1)$ K. As expected for superconductors, the critical temperature decreases systematically with increasing magnetic field, resulting in $T_c^{mag} = 3.4(1)$ K at $\mu_0 H = 8$ T. Furthermore, the transition width shows a progressive broadening with increasing magnetic field. This effect can be related to the high degree of chemical disorder and local strain variations inherent in the studied HEA, as evidenced by XRD analysis. The behavior of $\chi'(T)$ and $\chi''(T)$ dependencies of $(NbZr)_{0.75}(TiHf)_{0.25}$ and $(NbTi)_{0.75}(ZrHf)_{0.25}$ samples, in general, are qualitatively similar to those obtained for $(NbHf)_{0.75}(TiZr)_{0.25}$, indicating that both these HEAs exhibit superconductivity up to $\mu_0 H = 8$ T. However, T_c^{mag} measured at $\mu_0 H = 1$ mT is close to 7.8(2) K for $(NbTi)_{0.75}(ZrHf)_{0.25}$ and 8.0(2) K for $(NbZr)_{0.75}(TiHf)_{0.25}$. The measured transition temperatures differ significantly among the three HEAs despite their identical VEC values, revealing composition-dependent superconducting behavior. Worth mentioning is also the fact that T_c^{mag} determined for all three studied HEAs with VEC = 4.375 are comparable or even higher than those reported for VEC = 4.7 systems [8], despite the latter being previously predicted as optimal for maximizing T_c.

To gain further insight into the nature of the different critical temperatures, specific heat measurements were performed to characterize the fundamental superconducting properties.

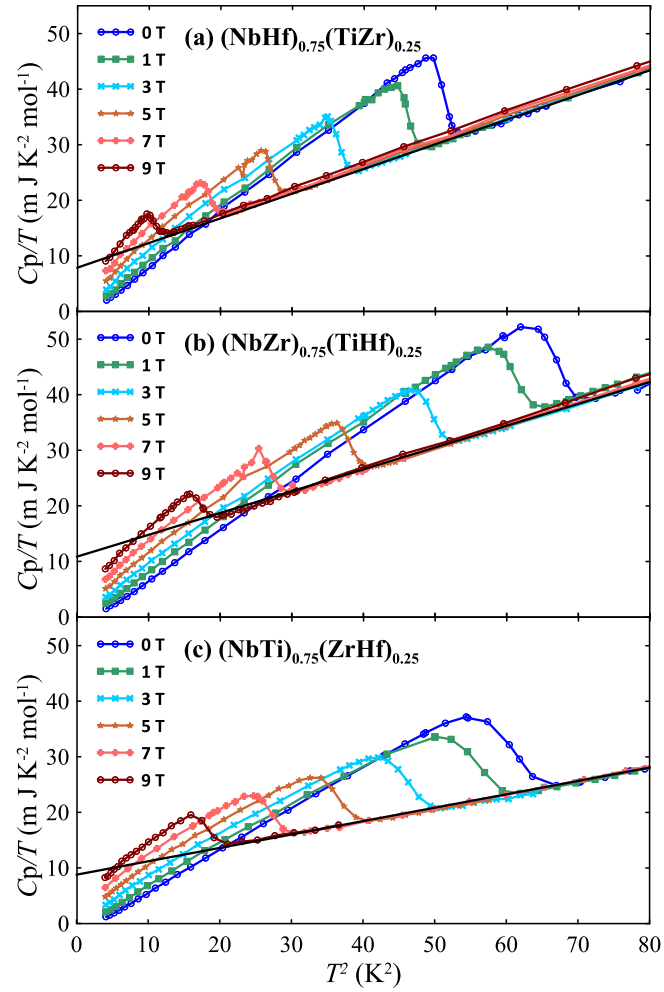

FIG. 3. Specific heat divided by temperature for (a) $(NbHf)_{0.75}(TiZr)_{0.25}$, (b) $(NbZr)_{0.75}(TiHf)_{0.25}$, and (c) $(NbTi)_{0.75}(ZrHf)_{0.25}$, as a function of T^2 measured at low temperatures and in various external magnetic fields. The black solid lines are fits of Eq. (2) to the experimental data.

Figure 3 presents the specific heat divided by temperature (C_p/T) of $(NbHf)_{0.75}(ZrTi)_{0.25}$, $(NbZr)_{0.75}(TiHf)_{0.25}$, and $(NbTi)_{0.75}(ZrHf)_{0.25}$, as a function of T^2 measured at low temperatures and in various external magnetic fields. The normal state-specific heat at low temperatures (above T_c) obeys the T^3-Debye law

$$\frac{C_p}{T} = \gamma + \beta T^2, \tag{2}$$

where the Sommerfeld coefficient γ represents the electronic contribution, and β is the phonon contribution to the specific heat. The density of states at the Fermi level, $N(E_F)$, was derived from the Sommerfeld coefficient via the relation

$$\gamma = \tfrac{1}{3}\pi^2 k_B^2 N_A N(E_F), \tag{3}$$

where k_B is the Boltzmann constant and N_A is the Avogadro's number. At the same time, the determined β value can be used to calculate the Debye temperature Θ_D^{LT} in the

TABLE I. Experimentally determined basic characteristic parameters of normal and superconducting states of $(NbHf)_{0.75}(TiZr)_{0.25}$, $(NbZr)_{0.75}(TiHf)_{0.25}$, and $(NbTi)_{0.75}(ZrHf)_{0.25}$ (for details see the text).

Parameters	$(NbHf)_{0.75}(TiZr)_{0.25}$	$(NbZr)_{0.75}(TiHf)_{0.25}$	$(NbTi)_{0.75}(ZrHf)_{0.25}$
Lattice parameter a [Å]	3.431(1)	3.426(1)	3.360(1)
Mean grain size L [nm]	101(7)	55(3)	94(6)
Level of internal strain $C\epsilon$ [%]	2.31(2)	2.48(3)	2.43(2)
Critical temperature (magnetic data) T_c^{mag} [K]	7.4(2)	8.0(2)	7.9(2)
Critical temperature (WHH) T_c [K]	7.15(5)	8.17(5)	7.76(5)
Sommerfeld coefficient γ [mJ K^{-2} mol^{-1}]	7.8(3)	10.8(9)	8.8(3)
Density of states at the Fermi level $N(E_F)$ [st. eV^{-1} f.u. $^{-1}$]	3.3(2)	4.6(4)	3.7(1)
Phonon contribution to the specific heat β [mJ K^{-4} mol^{-1}]	0.444(4)	0.393(9)	0.241(3)
Debye temperature Θ_D^{LT} [K]	164(1)	170(1)	201(1)
Electron-phonon coupling λ_{el-ph}	0.92(1)	0.97(1)	0.87(1)
Normalized specific heat jump $\Delta C/\gamma T_c$	2.22(8)	1.8(1)	2.02(7)
Normalized energy gap $2\Delta_0/(k_B T_c)$	4.68(8)	4.76(7)	3.88(3)
Lower critical field $\mu_0 H_{c1}(0)$ [mT]	9.7(3)	15.6(7)	8.2(2)
Thermodynamic critical field $\mu_0 H_c(0)$ [mT]	186(5)	255(11)	182(4)
Upper critical field $\mu_0 H_{c2}(0)$ [T]	12.5(4)	13.3(4)	14.0(9)
$[\frac{d(\mu_0 H_{c2}(T))}{dT}]_{T=T_c}$ [TK^{-1}]	−2.9(1)	−2.8(1)	−3.2(3)
Orbital-limiting field $\mu_0 H_{c2}^{orb}(0)$ [T]	14.3	15.8	17.2
Pauli limiting field $\mu_0 H_P$ [T]	13.14(9)	15.03(9)	14.28(9)
Maki parameter α_M	1.53(6)	1.47(5)	1.7(1)
Spin-orbit scattering constant λ_{SO}	3.1	2.0	2.1
Coherence length ξ_{GL} [nm]	4.8(1)	4.6(1)	4.4(2)
Magnetic penetration depth λ_{GL} [nm]	260(9)	199(9)	290(14)
Ginzburg-Landau parameter κ_{GL}	54	44	66

low-temperature regime from the equation

$$\Theta_D = \left(\frac{12R\pi^4}{5\beta}\right)^{\frac{1}{3}}, \tag{4}$$

where R is the molar gas constant. The determined values of γ, β, $N(E_F)$, and Θ_D^{LT} are summarized in Table I. As one can notice, a clear correlation emerges between enhanced electronic parameters and T_c, with $(NbZr)_{0.75}(TiHf)_{0.25}$ showing both the largest γ [10.8(9) mJ K^{-2} mol^{-1}] and $N(E_F)$ [4.6(4) states eV^{-1} f.u.$^{-1}$] values, along with the highest T_c. Thus, one can attribute the increasing of the critical temperature with an increasing of the density of states in HEAs under investigation. At the same time, the calculated Θ_D^{LT} show a clear dependence on the relative concentrations of Hf, Zr, and Ti. In particular, the Ti-rich HEA exhibits the highest $\Theta_D^{LT} = 201(1)$ K, followed by the Zr-rich [170(1) K] and Hf-rich [164(1) K] compositions. This trend can be related to the systematic decrease in Θ_D^{LT} observed for the pure metals (Ti → Zr → Hf) [31], suggesting a direct link between elemental composition and lattice stiffness in these HEAs.

The results presented in Fig. 3 reveal that all three alloys exhibit a single, well-defined superconducting transition, manifested as the specific-heat jump at their respective T_c, providing the emergence of a single collective superconducting phase. As expected, T_c is reduced with increasing magnetic field. However, for all studied alloys, the superconductivity is still observable above 2 K at 9 T, revealing exceptionally high upper critical fields. The determined ratios $\Delta C/\gamma T_c$, shown in Table I, exceed the standard weak-coupling BCS value of 1.43 [32], indicating intermediate- to strong-coupling superconductivity.

Analysis of the electronic low-temperature specific heat data enables determination of the superconducting energy gap (Δ_0) for all three HEAs within the framework of BCS theory [32]

$$C_{BCS}(T) = A\gamma T_c \exp\left(-\frac{\Delta_0}{k_B T}\right), \tag{5}$$

where A is a constant. The least-squares fit of Eq. (5) to the experimental data gave Δ_0 values from which the normalized energy gap $2\Delta_0/k_B T_C$ can be calculated. As one can see in Table I, all obtained $2\Delta_0/k_B T_C$ values are much higher than 3.52 predicted by the Bardeen-Cooper-Schrieffer (BCS) theory for a single and isotropic gap in the weak-coupling limit [32]. Furthermore, the electron-phonon coupling λ_{el-ph} can be evaluated using the approximated McMillan formula [33], which is applicable for $\lambda_{el-ph} < 1.25$ [34]

$$\lambda_{el-ph} = \frac{1.04 + \mu^* \ln\left(\frac{\Theta_D^{LT}}{1.45T_c}\right)}{(1 - 0.62\mu^*)\ln\left(\frac{\Theta_D^{LT}}{1.45T_c}\right) - 1.04}, \tag{6}$$

where $\mu^* = 0.125$ is the Coulomb pseudopotential. The derived coupling constants $\lambda_{el-ph} = 0.92(1)$ (Hf-rich), 0.97(1) (Zr-rich), and 0.84(1) (Ti-rich) classify these high-entropy alloys as intermediate-coupling superconductors. However, it should be noted that the values obtained for Hf-rich and Zr-rich compositions imply that these systems are very close to the strong-coupling regime ($\lambda_{el-ph} \geqslant 1$).

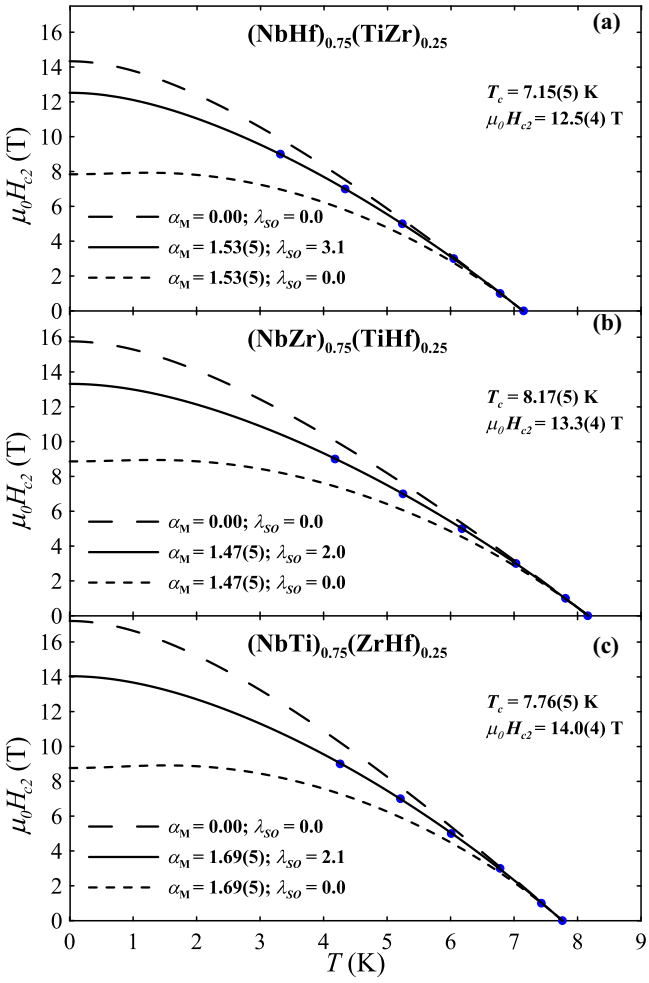

FIG. 4. Temperature dependence of the upper critical field $\mu_0 H_{c2}$ for (a) $(NbHf)_{0.75}(TiZr)_{0.25}$, (b) $(NbZr)_{0.75}(TiHf)_{0.25}$, and (c) $(NbTi)_{0.75}(ZrHf)_{0.25}$ derived from C_p data. The solid and dashed lines are fits of the WHH model [Eq. (7)] to the experimental data.

Using field-dependent specific heat measurements (Fig. 3), one can construct the superconducting phase diagrams for all three HEAs through analysis based on the Werthamer-Helfand-Hohenberg (WHH) model. The analysis employs the full WHH formalism for dirty-limit, isotropic-gap BCS superconductors, incorporating both the spin-paramagnetic effect (via the Maki parameter α_M) and spin-orbit scattering constant (λ_{SO}) to model the upper critical field behavior [35–37]

$$\ln\frac{1}{t} = \left(\frac{1}{2}+\frac{i\lambda_{SO}}{4\gamma_{WHH}}\right)\psi\left(\frac{1}{2}+\frac{\bar{h}+\frac{1}{2}\lambda_{SO}+i\gamma_{WHH}}{2t}\right) + \left(\frac{1}{2}-\frac{i\lambda_{SO}}{4\gamma_{WHH}}\right)\psi\left(\frac{1}{2}+\frac{\bar{h}+\frac{1}{2}\lambda_{SO}-i\gamma_{WHH}}{2t}\right) - \psi\left(\frac{1}{2}\right), \tag{7}$$

where $\gamma_{WHH} = \sqrt{(\alpha_M\bar{h})^2 - (\frac{1}{2}\lambda_{SO})^2}$, $\bar{h} = \frac{4}{\pi^2}\frac{H_{c2}}{-dH_{c2}/dt}$, $t = \frac{T}{T_c}$, ψ is a digamma function and i denotes the imaginary unit.

Figure 4 presents three theoretical predictions of the upper critical field: (i) the orbital-limited case [$\mu_0 H_{c2}^{orb}(T)$, neglecting both spin paramagnetism and spin-orbit effects]; (ii) an intermediate model incorporating only spin paramagnetism ($\alpha_M \neq 0, \lambda_{SO} = 0$); and (iii) the full WHH model [$\mu_0 H_{c2}(T)$] that best fits the experimental data by including both spin effects ($\alpha_M \neq 0, \lambda_{SO} \neq 0$). For each system, the temperature derivative of the upper critical field, $d\mu_0 H(T)/dT$, was extracted by linear regression of the data points closest to the critical temperature, while the Maki parameter was calculated using the relation [35]

$$\alpha_M = -0.528\left(\frac{d\mu_0 H(T)}{dT}\right)_{T=T_c}. \tag{8}$$

The Pauli limiting field $\mu_0 H_P$ was calculated according to the formula [38,39]

$$\mu_0 H_P = 1.84 T_c, \tag{9}$$

using the critical temperature obtained from the full WHH model. The determined values of T_c, $\mu_0 H_{c2}(0)$, $\mu_0 H_{c2}^{orb}(0)$, $\mu_0 H_P$, α_M, and λ_{SO} are summarized in Table I. It is noteworthy that for all studied HEAs $\mu_0 H_{c2}(0)$ are higher than 12 T. In particular, $\mu_0 H_{c2}(0) = 14.0(9)$ T obtained for the $(NbTi)_{0.75}(ZrHf)_{0.25}$ composition, is one of the highest reported values among the known bcc-structured HEA superconductors [4,5,40]. This enhanced upper critical field can be attributed to the high Nb and Ti content, consistent with the recent report of exceptionally high $\mu_0 H_{c2}(0) = 13.5(1)$ T found in the Ti-rich HEA superconductor $Ti_{0.5}(ZrNbHfTa)_{0.5}$ [41]. Finally, it must be mentioned that many upper critical field values, reported in works [4,5,40,42], were derived from resistivity measurements rather than specific heat data. Furthermore, these $\mu_0 H_{c2}(0)$ values were determined using the onset criterion of the resistivity curves or using simplified analysis methods that omit the full WHH formalism. Such methodological approaches may systematically overestimate the resulting upper critical fields, as they do not fully account for superconducting fluctuations and spin-coupling effects.

The thermodynamic critical field at 0 K $\mu_0 H_c(0)$ was derived from the superconducting energy gap Δ_0 and the Sommerfeld coefficient γ_{cgs}, using the relation [43]

$$\mu_0 H_c(0) = \sqrt{\frac{3\gamma_{cgs}\mu_0}{2\pi^2}}\frac{\Delta_0}{k_B}, \tag{10}$$

where γ_{cgs} is expressed in erg cm^{-3} K^{-2}. The obtained values of $\mu_0 H_{c2}^{orb}(0)$ and $\mu_0 H_c(0)$ allow the determination of two fundamental superconducting length scales, namely the magnetic penetration depth λ_{GL} and the Ginzburg-Landau coherence length ξ_{GL} [44]:

$$\xi_{GL} = \sqrt{\frac{\phi_0}{2\pi\mu_0 H_{c2}^{orb}(0)}} \quad \text{and} \quad \lambda_{GL} = \sqrt{\frac{\phi_0}{4\pi}\frac{\mu_0 H_{c2}^{orb}(0)}{\mu_0 H_c(0)^2}}, \tag{11}$$

where $\phi_0 = 2.067\times10^{-15}$ Wb is the magnetic flux quantum. Consequently, the Ginzburg-Landau parameter $\kappa_{GL} = \lambda_{GL}/\xi_{GL}$ was obtained and used to estimate the lower critical field at 0 K $\mu_0 H_{c1}(0)$ according to the equation [44]

$$\mu_0 H_{c1}(0) = \frac{H_c(0)}{\sqrt{2}\kappa_{GL}}\ln\kappa_{GL}. \tag{12}$$

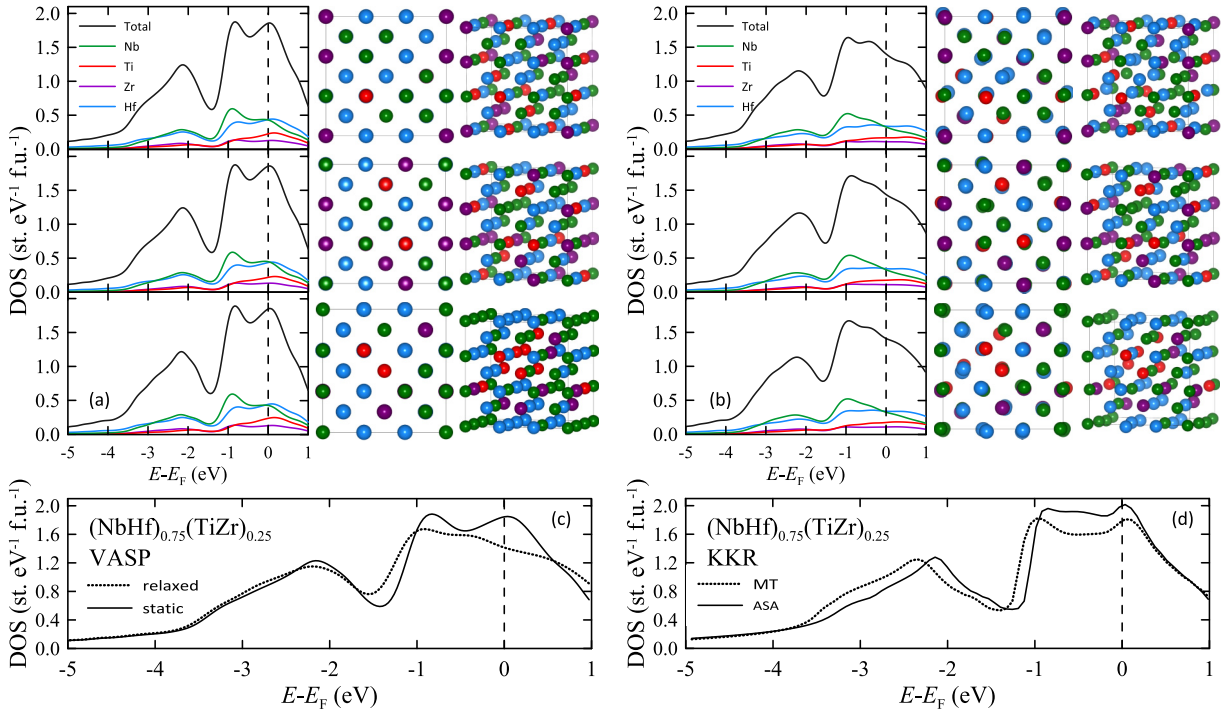

FIG. 5. Total and partial atomic densities of states of $(NbHf)_{0.75}(TiZr)_{0.25}$ calculated by the PAW method using VASP for three assumed random atomic arrangements (supercells shown at the right panel). (a) Depicts static configuration and (b) after additional ions relaxation. Lower panels present comparison between TDOS (c) averaged over three configurations by PAW and (d) calculated using KKR-CPA.

The calculated values of $\mu_0 H_{c1}(0)$, $\mu_0 H_c(0)$, λ_{GL}, ξ_{GL}, and κ_{GL} are listed in Table I. In particular, κ_{GL} values determined for all three HEAs significantly exceed the $1/\sqrt{2}$ limit, confirming that these materials are type-II superconductors. It is worth noting that the microscopic origins of the exceptionally high $\mu_0 H_{c2} = 14.0(9)$ T observed in the Ti-rich alloy can be related to the combined effects of: (1) nanoscale coherence length ($\xi_{GL} = 4.4$ nm) caused by atomic disorder and lattice strain; (2) strong spin-orbit coupling which can reduce the Pauli paramagnetic limiting effect [$\lambda_{SO} = 2.1$ and $\alpha_M = 1.7(1)$].

C. Theoretical results

Figures 5(a) and 5(b) present total and partial atomic densities of states calculated by the PAW method using VASP for three assumed random atomic arrangements (supercells shown on the right panel) for the pristine and relaxed $(NbHf)_{0.75}(TiZr)_{0.25}$ system, respectively. In general, the high similarity of the results for the three distinct atomic arrangements suggests that the influence of the local atomic configuration on the electronic structure of HEAs near the Fermi level (E_F) is small or even negligible. This finding agrees with earlier PAW-method results for various high-entropy alloys [41,45,46]. Consequently, the total density of states (TDOS), averaged over the three atomic configurations, was computed for each system and is shown in Fig. 5(c). The data clearly show that the TDOS of the pristine (unrelaxed) structure differs significantly from that of the relaxed system. Specifically, static TDOS exhibits two broad peaks near the Fermi level, with maxima at -0.9 eV and $+0.2$ eV relative to E_F. After ionic relaxation, both peaks are substantially reduced and broadened, likely due to increased structural and electronic disorder from atomic rearrangements. At the same time, the density of states at the Fermi level, $N^{th}(E_F)$, decreases significantly from 1.84 to 1.42 st. eV^{-1} f.u.$^{-1}$. The TDOS for $(NbHf)_{0.75}(TiZr)_{0.25}$, calculated using the KKR-CPA method within MT approximation and atomic spherical approximation (ASA), are presented in Fig. 5(c). The total density of states obtained from KKR-CPA (with MT approximation) agrees well with PAW-calculated results for the pristine system, yielding $N^{th}(E_F) = 1.78$ st. eV^{-1} f.u.$^{-1}$. In the case of KKR-CPA method with ASA, one can notice that TDOS values are systematically elevated near the Fermi level, in particular $N^{th}(E_F) = 2$ st. eV^{-1} f.u.$^{-1}$.

The obtained $N(E_F)$ and $N^{th}(E_F)$ values can be used to calculate λ^{th}_{el-ph} parameter by the following considerations. In general, the ratio between experimentally and theoretically determined Sommerfeld coefficients γ_{exp}/γ_{th} is equal to [31,47]

$$\frac{\gamma_{exp}}{\gamma_{th}} = \frac{m^*}{m_b}, \tag{13}$$

where m^* is the thermal effective mass of electron which is a measure of an average of the electron velocity over the Fermi surface, and m_b denotes a bare or band structure effective mass, where only effects due to the crystal potential, that is band structure effects, have been included. In real materials, the thermal effective mass deviates from the band mass due to many-body interactions, quantified by electron-phonon (λ_{el-ph}) and electron-electron (λ_{el-el}) enhancement

TABLE II. Basic characteristic parameters of the normal and superconducting states of $(NbHf)_{0.75}(TiZr)_{0.25}$, $(NbZr)_{0.75}(TiHf)_{0.25}$ and $(NbTi)_{0.75}(ZrHf)_{0.25}$ derived from first-principles calculations (for details see the text).

Parameters	$(NbHf)_{0.75}(TiZr)_{0.25}$	$(NbZr)_{0.75}(TiHf)_{0.25}$	$(NbTi)_{0.75}(ZrHf)_{0.25}$
KKR-CPA (ASA)			
Lattice parameter a [Å]	3.539	3.522	3.438
Bulk modulus B [GPa]	104.4	117.1	119.6
Pressure derivative B'	3.27	3.23	3.57
Density of states at the Fermi level $N^{\mathrm{th}}(E_{\mathrm{F}})$ [st. eV^{-1} f.u.$^{-1}$]	2.00	1.98	1.98
Electron-phonon coupling $\lambda^{\mathrm{th}}_{\mathrm{el-ph}}$	0.67(7)	1.33(19)	0.88(7)
KKR-CPA (MT)			
Lattice parameter a [Å]	3.425	3.447	3.375
Bulk modulus B [GPa]	113.1	109.3	116.3
Pressure derivative B'	3.52	3.18	3.75
Density of states at the Fermi level $N^{\mathrm{th}}(E_{\mathrm{F}})$ [st. eV^{-1} f.u.$^{-1}$]	1.78	1.82	1.84
Electron-phonon coupling $\lambda^{\mathrm{th}}_{\mathrm{el-ph}}$	0.87(8)	1.52(21)	1.02(13)
static PAW (averaged over three configurations)			
Lattice parameter a [Å]	3.423(1)	3.430(1)	3.356(1)
Bulk modulus B [GPa]	119.2(1)	115.2(1)	119.5(1)
Pressure derivative B'	3.20(1)	3.15(1)	3.44(1)
Density of states at the Fermi level $N^{\mathrm{th}}(E_{\mathrm{F}})$ [st. eV^{-1} f.u.$^{-1}$]	1.84(1)	1.84(3)	1.92(2)
Electron-phonon coupling $\lambda^{\mathrm{th}}_{\mathrm{el-ph}}$	0.81(8)	1.50(21)	0.94(7)
relaxed PAW (averaged over three configurations)			
Density of states at the Fermi level $N^{\mathrm{th}}(E_{\mathrm{F}})$ [st. eV^{-1} f.u.$^{-1}$]	1.42(2)	1.47(1)	1.57(3)
Electron-phonon coupling $\lambda^{\mathrm{th}}_{\mathrm{el-ph}}$	1.35(11)	2.13(26)	1.37(9)

terms

$$m^* = m_{\mathrm{b}}(1 + \lambda_{\mathrm{el-ph}} + \lambda_{\mathrm{el-el}}). \tag{14}$$

Combining this with Eq. (13) one can obtain the total coupling strength

$$\lambda_{\mathrm{el-ph}} + \lambda_{\mathrm{el-el}} = \frac{m^*}{m_{\mathrm{b}}} - 1 = \frac{\gamma_{\mathrm{exp}}}{\gamma_{\mathrm{th}}} - 1 = \frac{N(E_{\mathrm{F}})}{N^{\mathrm{th}}(E_{\mathrm{F}})} - 1. \tag{15}$$

Assuming a negligibly small influence of electron-electron interactions ($\lambda_{\mathrm{el-el}} \approx 0$), which is well justified for conventional metallic systems, it is possible to estimate $\lambda^{\mathrm{th}}_{\mathrm{el-ph}}$ using $N(E_{\mathrm{F}})$ and $N^{\mathrm{th}}(E_{\mathrm{F}})$ values.

The theoretically derived values of the lattice parameter (a), bulk modulus (B), its pressure derivative (B'), $N^{\mathrm{th}}(E_{\mathrm{F}})$ and $\lambda^{\mathrm{th}}_{\mathrm{el-ph}}$ for $(NbHf)_{0.75}(TiZr)_{0.25}$, obtained from DFT calculations, are listed in Table II. As one can see, among the four computational methods employed, the KKR-CPA (with MT approximation) and static PAW approaches yielded $\lambda^{\mathrm{th}}_{\mathrm{el-ph}}$ in good agreement with the experimental value of 0.92(1). In contrast, KKR-CPA with ASA method significantly underestimates $\lambda^{\mathrm{th}}_{\mathrm{el-ph}}$, probably due to the oversimplification of potential shapes. In the case of relaxed PAW approach, the resulting $\lambda^{\mathrm{th}}_{\mathrm{el-ph}} = 1.35$ is significantly higher than the experimental one. Similar result were recently reported for $Ti_{0.5}(ZrNbHfTa)_{0.5}$ and $Ti_{0.5}(VNbHfTa)_{0.5}$ superconducting HEAs, where relaxed PAW approach predicted $\lambda^{\mathrm{th}}_{\mathrm{el-ph}}$ values almost two times higher than the static PAW results and about 20% higher than experimentally determined $\lambda_{\mathrm{el-ph}}$ for as-cast samples [41]. These discrepancies suggest that while arc-melted (nonannealed) HEA samples retain kinetically trapped atomic configurations, the PAW relaxation artificially optimizes local ionic environments, decreasing $N^{\mathrm{th}}(E_{\mathrm{F}})$ and increasing $\lambda^{\mathrm{th}}_{\mathrm{el-ph}}$. Therefore, one can state that PAW method with ions relaxation is unsuitable for modeling the electronic structure of arc-melted HEAs, leading to unphysical overestimation of key parameters like $\lambda^{\mathrm{th}}_{\mathrm{el-ph}}$. For these systems, static PAW or KKR-CPA approaches provide quantitatively more accurate predictions of their electronic structure.

The electronic structure of $(NbZr)_{0.75}(TiHf)_{0.25}$, calculated using the KKR-CPA and PAW methods, is shown in Fig. 6. In general, the results obtained for this HEA is comparable to that determined for $(NbHf)_{0.75}(TiZr)_{0.25}$. In particular, the KKR-CPA and static PAW approaches reveal two TDOS maxima near E_{F}, while after ionic relaxation, both peaks are substantially reduced and broadened. Basic characteristic parameters of $(NbZr)_{0.75}(TiHf)_{0.25}$ derived from first-principles calculations are listed in Table II. It can be seen that all computational methods systematically overestimate the electron-phonon coupling constant compared to the experiment, yielding theoretical values $\lambda^{\mathrm{th}}_{\mathrm{el-ph}} = 1.33$–$2.13$ against experimental $\lambda_{\mathrm{el-ph}} = 0.97(1)$. However, these results reproduce the trends observed in $(NbHf)_{0.75}(TiZr)_{0.25}$ data, i.e., the values of $\lambda^{\mathrm{th}}_{\mathrm{el-ph}}$ obtained from KKR-CPA and static PAW are consistent within uncertainties, while the relaxed PAW approach again significantly overestimates the electron-phonon coupling constant.

Figure 7 compares the electronic structure of $(NbTi)_{0.75}(ZrHf)_{0.25}$ derived from KKR-CPA and PAW calculations. In the case of KKR-CPA and static PAW approaches, the TDOS maximum is located around 0.1 eV above E_{F}, with dominant contribution from Ti $3d$-electron states. At the same time, TDOS determined for relaxed

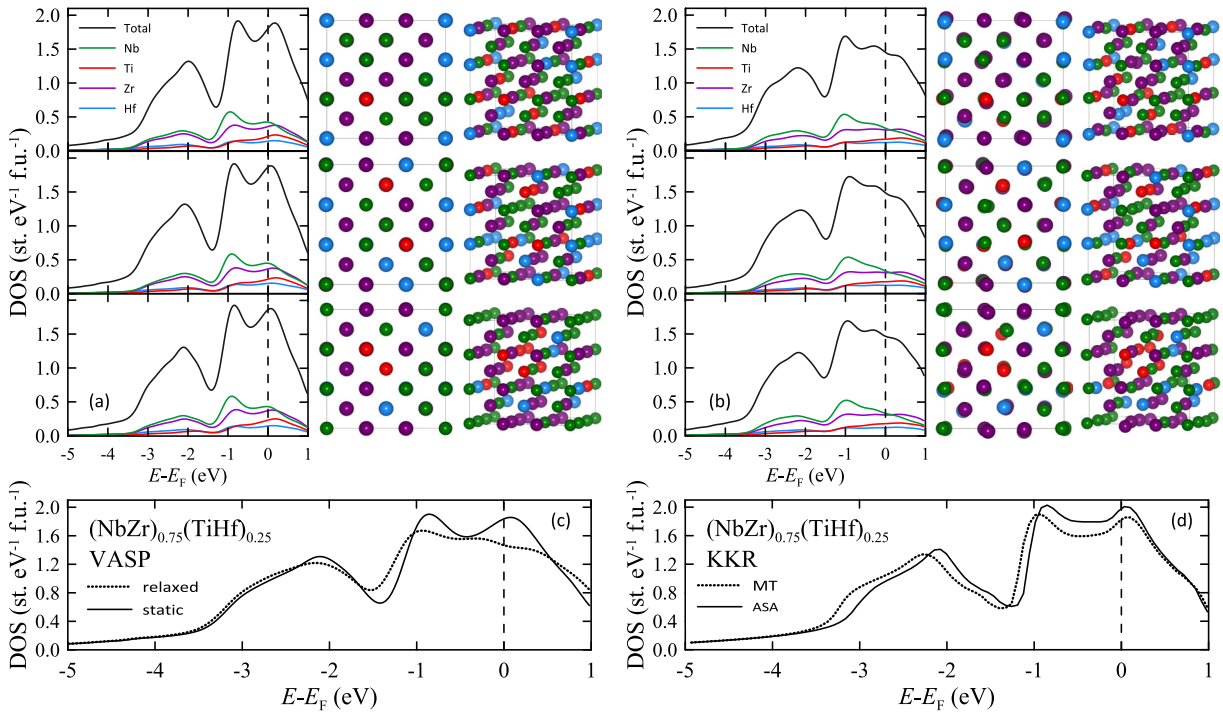

FIG. 6. Total and partial atomic densities of states of $(NbZr)_{0.75}(TiHf)_{0.25}$ calculated by the PAW method using VASP for three assumed random atomic arrangements (supercells shown at the right panel). (a) Depicts static configuration and (b) after additional ions relaxation. Lower panels present comparison between TDOS (c) averaged over three configurations by PAW and (d) calculated using KKR-CPA.

structure exhibits a broad band in the Fermi energy region with maximum at 1 eV below E_F. The estimated values of λ^{th}_{el-ph}, which are listed in Table II, confirms our previous observations that KKR-CPA and static PAW give consistent λ^{th}_{el-ph} values within uncertainties and in the case of $(NbTi)_{0.75}(ZrHf)_{0.25}$ they are in well agreement

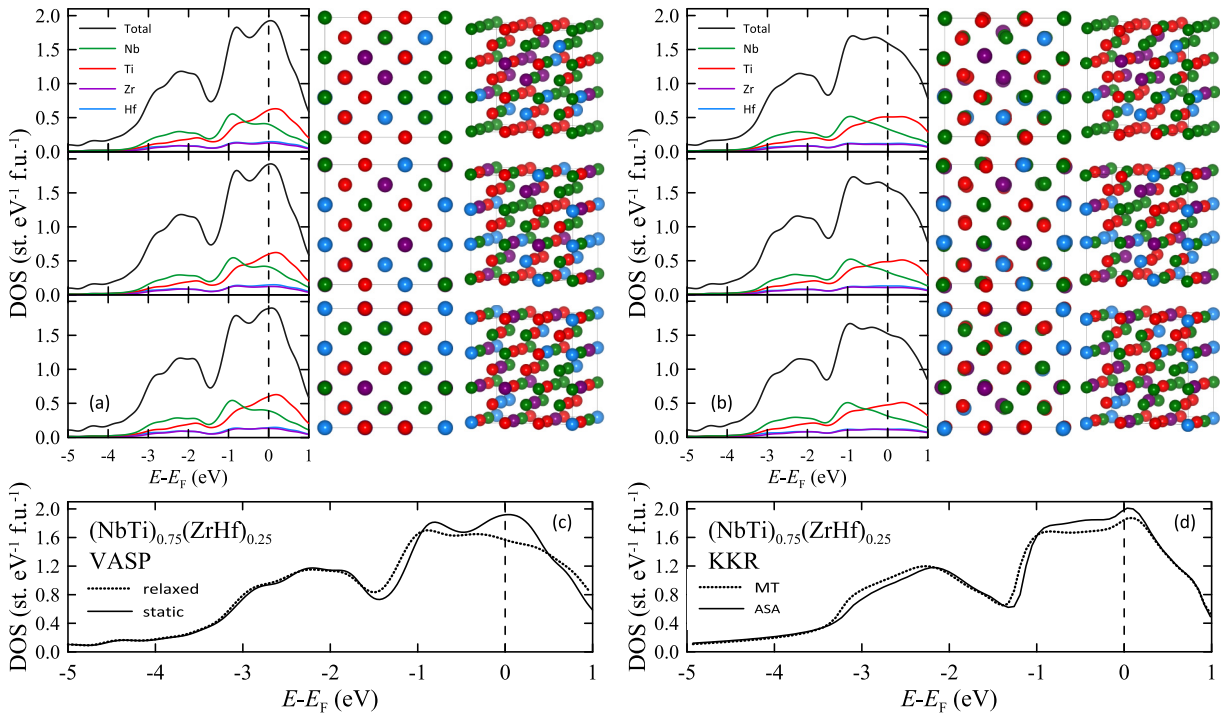

FIG. 7. Total and partial atomic densities of states of $(NbTi)_{0.75}(ZrHf)_{0.25}$ calculated by the PAW method using VASP for three assumed random atomic arrangements (supercells shown at the right panel). (a) Depicts static configuration and (b) after additional ions relaxation. Lower panels present comparison between TDOS (c) averaged over three configurations by PAW and (d) calculated using KKR-CPA.

with the experimental value of 0.87(1). For the relaxed system, the theoretical electron-phonon coupling constant $\lambda_{el-ph}^{th} = 1.37(9)$ significantly exceeds experimental value, highlighting the systematic overestimation inherent in ionic relaxation approaches to HEAs.

IV. CONCLUSION

Our comparative study of three bcc-type HEAs $(NbHf)_{0.75}(TiZr)_{0.25}$, $(NbZr)_{0.75}(TiHf)_{0.25}$, and $(NbTi)_{0.75}(ZrHf)_{0.25}$, with a fixed valence electron count (VEC = 4.375), demonstrates that elemental composition, rather than VEC alone, governs superconducting behavior. Despite identical VEC, critical temperatures T_c vary significantly (7.14–8.17 K), correlating directly with the density of states at the Fermi level $N(E_F)$. The Zr-rich alloy $(NbZr)_{0.75}(TiHf)_{0.25}$ exhibits the highest $N(E_F) = 4.6(4)$ states $eV^{-1}\,f.u.^{-1}$ and $T_c = 8.17(5)$ K, while the lowest parameters, $N(E_F) = 3.3(2)$ states $eV^{-1}\,f.u.^{-1}$ and $T_c = 7.14(5)$ K, are observed for $(NbHf)_{0.75}(TiZr)_{0.25}$.

All alloys exhibit exceptionally high upper critical fields [$\mu_0 H_{c2}(0) > 12$ T], with the Ti-rich $(NbTi)_{0.75}(ZrHf)_{0.25}$ achieving $\mu_0 H_{c2}(0) = 14.0(9)$ T, which one of the highest reported for bcc HEAs. This performance can be attributed to nanoscale coherence lengths [$\xi_{GL} = 4.4(2)$ nm] and strong spin-orbit coupling ($\lambda_{SO} = 2.1$), which reduce the effect of Pauli paramagnetic limiting.

First-principles calculations reveal critical methodological insights: while the electron-phonon coupling constant values obtained using KKR-CPA and static PAW methods are close to the experimental values, those obtained using relaxed projector augmented-wave (PAW) are overestimated. This discrepancy arises from the artificial optimization of local ionic positions in the PAW method, meaning that static approaches better model the electronic structure of nonannealed HEA systems.

These results redefine the design principles of bcc-type high-entropy alloy superconductors by demonstrating that the Matthias rule is not the main factor in determining their superconducting properties. Rather, achieving an optimal critical temperature (T_c) and an optimal upper critical field [$\mu_0 H_{c2}(0)$] requires the enrichment of Nb and Ti, elements that enhance the electronic density of states at the Fermi level while maintaining structural stability. The exceptional properties observed in Ti-rich composition suggests that Nb and Ti are critical elements for developing next-generation superconductors. Future studies should, therefore, systematically investigate Nb- and Ti-rich HEAs to exploit their potential in high-field magnet technologies.

ACKNOWLEDGMENTS

This work was financed by the National Science Centre (Poland) under the OPUS 20 Project No. 2020/39/B/ST5/01782. We gratefully acknowledge Polish high performance computing infrastructure PLGrid (HPC Centers: ACK Cyfronet AGH, WCSS) for providing computer facilities and support within computational Grants No. PLG/2023/016716 and No. PLG/2024/017030. R.T. acknowledges the support of Dioscuri program initiated by the Max Planck Society, jointly managed with the National Science Centre (Poland), and mutually funded by the Polish Ministry of Science and Higher Education and the German Federal Ministry of Education and Research.

DATA AVAILABILITY

The data that support the findings of this article are openly available [48].

[1] J.-W. Yeh, S.-K. Chen, S.-J. Lin, J.-Y. Gan, T.-S. Chin, T.-T. Shun, C.-H. Tsau, and S.-Y. Chang, Nanostructured high-entropy alloys with multiple principal elements: Novel alloy design concepts and outcomes, Adv. Eng. Mater. **6**, 299 (2004).

[2] B. Cantor, I. Chang, P. Knight, and A. Vincent, Microstructural development in equiatomic multicomponent alloys, Mater. Sci. Eng.: A **375-377**, 213 (2004).

[3] P. Koželj, S. Vrtnik, A. Jelen, S. Jazbec, Z. Jagličić, S. Maiti, M. Feuerbacher, W. Steurer, and J. Dolinšek, Discovery of a superconducting high-entropy alloy, Phys. Rev. Lett. **113**, 107001 (2014).

[4] L. Sun and R. J. Cava, High-entropy alloy superconductors: Status, opportunities, and challenges, Phys. Rev. Mater. **3**, 090301 (2019).

[5] L. Zeng, L. Li, K. Li, R. Chen, and H. Luo, Recent advances in high-entropy superconductors, NPG Asia Mater. **16**, 60 (2024).

[6] J. Kitagawa, Y. Mizuguchi, and T. Nishizaki, High critical current densities of body-centered cubic high-entropy alloy superconductors: Recent research progress, Eur. Phys. J. B **98**, 73 (2025).

[7] B. T. Matthias, Empirical relation between superconductivity and the number of valence electrons per atom, Phys. Rev. **97**, 74 (1955).

[8] F. von Rohr, M. J. Winiarski, J. Tao, T. Klimczuk, and R. J. Cava, Effect of electron count and chemical complexity in the Ta-Nb-Hf-Zr-Ti high-entropy alloy superconductor, Proc. Natl. Acad. Sci. USA **113**, E7144 (2016).

[9] L. Zeng, J. Zhan, M. Boubeche, K. Li, L. Li, P. Yu, K. Wang, C. Zhang, K. Jin, Y. Sun, and H. Luo, Superconductivity in the bcc-type high-entropy alloy TiHfNbTaMo, Adv. Quantum Technol. **6**, 2300213 (2023).

[10] F. O. von Rohr and R. J. Cava, Isoelectronic substitutions and aluminium alloying in the Ta-Nb-Hf-Zr-Ti high-entropy alloy superconductor, Phys. Rev. Mater. **2**, 034801 (2018).

[11] J. Rodríguez-Carvajals, Recent advances in magnetic structure determination by neutron powder diffraction, Phys. B: Condens. Matter **192**, 55 (1993).

[12] P. Soven, Coherent-potential model of substitutional disordered alloys, Phys. Rev. **156**, 809 (1967).

[13] G. D. Gaspari and B. L. Gyorffy, Electron-phonon interactions, *d* resonances, and superconductivity in transition metals, Phys. Rev. Lett. **28**, 801 (1972).

[14] W. H. Butler, Theory of electronic transport in random alloys: Korringa-Kohn-Rostoker coherent-potential approximation, Phys. Rev. B **31**, 3260 (1985).
[15] S. Kaprzyk and A. Bansil, Green's function and a generalized Lloyd formula for the density of states in disordered muffin-tin alloys, Phys. Rev. B **42**, 7358 (1990).
[16] A. Bansil and S. Kaprzyk, First-principles treatment of disorder effects in complex alloys: A study of $Ba_xK_{1-x}BiO_3$ and $BaPb_{1-x}Bi_xO_3$, Phys. Rev. B **43**, 10335 (1991).
[17] H. Akai, Electronic structure Ni–Pd alloys calculated by the self-consistent KKR-CPA method, J. Phys. Soc. Jpn. **51**, 468 (1982).
[18] H. Akai, Fast Korringa-Kohn-Rostoker coherent potential approximation and its application to FCC Ni-Fe systems, J. Phys.: Condens. Matter **1**, 8045 (1989).
[19] T. Kotani and H. Akai, KKR-ASA method in exact exchange-potential band-structure calculations, Phys. Rev. B **54**, 16502 (1996).
[20] J. P. Perdew and W. Yue, Accurate and simple density functional for the electronic exchange energy: Generalized gradient approximation, Phys. Rev. B **33**, 8800 (1986).
[21] J. P. Perdew, K. Burke, and M. Ernzerhof, Generalized gradient approximation made simple, Phys. Rev. Lett. **77**, 3865 (1996).
[22] J. P. Perdew, K. Burke, and Y. Wang, Generalized gradient approximation for the exchange-correlation hole of a many-electron system, Phys. Rev. B **54**, 16533 (1996).
[23] F. Birch, Finite elastic strain of cubic crystals, Phys. Rev. **71**, 809 (1947).
[24] G. Kresse and J. Hafner, *Ab initio* molecular dynamics for open-shell transition metals, Phys. Rev. B **48**, 13115 (1993).
[25] G. Kresse and J. Furthmüller, Efficient iterative schemes for *ab initio* total-energy calculations using a plane-wave basis set, Phys. Rev. B **54**, 11169 (1996).
[26] G. Kresse and J. Furthmüller, Efficiency of *ab initio* total energy calculations for metals and semiconductors using a plane-wave basis set, Comput. Mater. Sci. **6**, 15 (1996).
[27] G. Kresse and D. Joubert, From ultrasoft pseudopotentials to the projector augmented-wave method, Phys. Rev. B **59**, 1758 (1999).
[28] P. E. Blöchl, Projector augmented-wave method, Phys. Rev. B **50**, 17953 (1994).
[29] O. N. Senkov, J. M. Scott, S. V. Senkova, D. B. Miracle, and C. F. Woodward, Microstructure and room temperature properties of a high-entropy TaNbHfZrTi alloy, J. Alloys Compd. **509**, 6043 (2011).
[30] G. Williamson and W. Hall, X-ray line broadening from filed aluminium and wolfram, Acta Metall. **1**, 22 (1953).
[31] A. Tari, *The Specific Heat of Matter at Low Temperatures* (World Scienfitic, Singapore, 2003).
[32] J. Bardeen, L. N. Cooper, and J. R. Schrieffer, Theory of superconductivity, Phys. Rev. **108**, 1175 (1957).
[33] W. L. McMillan, Transition temperature of strong-coupled superconductors, Phys. Rev. **167**, 331 (1968).
[34] P. B. Allen and R. C. Dynes, Transition temperature of strong-coupled superconductors reanalyzed, Phys. Rev. B **12**, 905 (1975).
[35] E. Helfand and N. R. Werthamer, Temperature and purity dependence of the superconducting critical field, H_{c2}. II, Phys. Rev. **147**, 288 (1966).
[36] N. R. Werthamer, E. Helfand, and P. C. Hohenberg, Temperature and purity dependence of the superconducting critical field, H_{c2}. III. electron spin and spin-orbit effects, Phys. Rev. **147**, 295 (1966).
[37] K. Maki, Effect of Pauli paramagnetism on magnetic properties of high-field superconductors, Phys. Rev. **148**, 362 (1966).
[38] A. M. Clogston, Upper limit for the critical field in hard superconductors, Phys. Rev. Lett. **9**, 266 (1962).
[39] Y. Shapira and L. J. Neuringer, Upper critical fields of Nb-Ti alloys: Evidence for the influence of Pauli paramagnetism, Phys. Rev. **140**, A1638 (1965).
[40] J. Kitagawa and Y. Mizuguchi, *High-Entropy Alloy Superconductors: Exotic Properties, Applications and Materials Design*, Springer Series in Solid-State Sciences (Springer Nature, Singapore, 2024).
[41] P. Sobota, B. Rusin, D. Gnida, R. Topolnicki, T. Ossowski, W. Nowak, A. Pikul, and R. Idczak, New type of Ti-rich HEA superconductors with high upper critical field, Acta Mater. **285**, 120666 (2025).
[42] M. Krnel, A. Jelen, S. Vrtnik, J. Luzar, D. Gačnik, P. Koželj, M. Wencka, A. Meden, Q. Hu, S. Guo, and J. Dolinšek, The effect of scandium on the structure, microstructure and superconductivity of equimolar Sc-Hf-Nb-Ta-Ti-Zr refractory high-entropy alloys, Materials **15**, 1122 (2022).
[43] R. D. Parks, *Superconductivity: In Two Volumes: Volume 1* (Taylor & Francis, New York, 2019).
[44] M. Tinkham, *Introduction to Superconductivity*, International series in pure and applied physics (McGraw-Hill, New York, 1975).
[45] P. Sobota, R. Topolnicki, T. Ossowski, T. Pikula, A. Pikul, and R. Idczak, Superconductivity in the high-entropy alloy $(NbTa)_{0.67}(MoHfW)_{0.33}$, Phys. Rev. B **106**, 184512 (2022).
[46] R. Idczak, W. Nowak, B. Rusin, R. Topolnicki, T. Ossowski, M. Babij, and A. Pikul, Enhanced superconducting critical parameters in a new high-entropy alloy $Nb_{0.34}Ti_{0.33}Zr_{0.14}Ta_{0.11}Hf_{0.08}$, Materials **16**, 5814 (2023).
[47] C. Kittel, *Introduction to Solid State Physics*, 7th ed. (Wiley, New York, 2007).
[48] OSF repository at https://osf.io/g4n6b/.